S.I. DRAPAK,[1, 2] S.V. GAVRYLYUK,[3] Y.B. KHALAVKA,[2] V.D. FOTIY,[1]
P.M. FOCHUK,[2] O.I. FEDIV [4]

[1] Photon-Quartz Design and Technology Ltd.
  (246, Golovna Str., Chernivtsi 58032, Ukraine; e-mail: sdrapak@ukr.net)
[2] Institute of Biology, Chemistry and Bioresources,
  Yuriy Fedkovych National University of Chernivtsi
  (25, Lesi Ukrainky Str., Chernivtsi 58012, Ukraine)
[3] Institute of Applied Mathematics and Fundamental Sciences,
  National University "Lviv Polytechnic"
  (12, S. Bandery Str., Lviv 79013, Ukraine)
[4] Bukovinian State Medical University
  (2, Teatralna Sq., Chernivtsi 58000, Ukraine)

CHARACTERIZATION OF NANOSTRUCTURED In_6Se_7 INCLUSIONS IN LAYERED α-In_2Se_3 CRYSTALS USING ANALYTICAL X-RAY DIFFRACTOMETRY METHODS

As follows from the X-ray structural analysis, In_2Se_3 crystals grown from the stoichiometric melt using the Bridgman method turned out inhomogeneous: some of the samples obtained from the same ingot contained only the hexagonal α-In_2Se_3 phase, whereas inclusions of the In_6Se_7 crystalline phase were found in the others. The presence of narrower-band-gap semiconductor inclusions in the α-In_2Se_3 matrix gives rise to the current instability with Z- and N-shaped current-voltage characteristics (CVCs) of the samples; at the same time, single-phase samples demonstrate linear CVCs. Several analytical methods of X-ray diffraction (XRD) analysis, which were applied to characterize the structure of In_6Se_7 inclusions, testified to the presence of compressive strains in them. It is shown that, owing to the action of compressive strains, the average sizes of In_6Se_7 crystallites determined using the modified Scherrer, Size-Strain Plot, and Halder–Wagner methods coincide with an accuracy higher than 1% and equal about 26.5 nm. A discrepancy between this value and the average size of In_6Se_7 nanocrystallites determined using the Williamson–Hall method (23.13 nm) has been discussed. With the help of the X-ray diffraction-absorption method, the average mass fraction of the In_6Se_7 phase in the investigated samples is determined, and the average concentration of In_6Se_7 nanocrystallites with an average size of about 26.5 nm over the volume of the layered α-In_2Se_3 matrix is calculated. A perspective character of the application of In_2Se_3/In_6Se_7 composite samples for operating in the optical telecommunication wavelength interval is discussed.

K e y w o r d s: layered In_2Se_3 crystals, microstructure, nanocrystallite inclusions, composites, analytical X-ray diffractometry methods.

1. Introduction

The binary inorganic compound of indium and selenium with the formula In_2Se_3 is a promising semiconductor material for the creation of photodetectors [1–3], photodiodes [4–6], and solar elements [7–9]. Indium selenide (In_2Se_3) is considered as a cathode material for lithium and lithium-ion current

sources [10, 11] and as an effective photocatalyst for the water decomposition into oxygen and hydrogen [12, 13]. The reverse change of crystalline structure under the action of electrical pulses [14] or pressure [15] makes it possible to predict the application of this semiconductor for the manufacture of phase-change memory (PCM). Ferromagnetism detected in nanosized In_2Se_3 objects at room temperature [16,17] testifies to the feasibility of the application of this compound in spintronics. The prospects of using In_2Se_3

as a material for thermocouples were discussed in works [18, 19].

In_2Se_3 is believed to be an intrinsically defective material. The structural imperfection of In_2Se_3 arises, because only two thirds of its cation sublattice sites are occupied by metal atoms. The intrinsic imperfection, possible deviations from stoichiometry, foreign impurities, various violations in the lattice structure regularity, and polytypism – all those factors bring about a situation when the results of physical research of the properties of In_2Se_3 crystals, films, or nanoscale objects are poorly consistent with one another and depend on the fabrication technology and the post-growth processing of the material.

Several structural modifications of In_2Se_3 are known [20, 21]. These are α-, β-, γ-, δ-, and k-modifications, which are different in their crystalline structures, as well as electric, dielectric, optical, and others properties. In work [22], the object of research was thin In_2Se_3 films of the g-polytype; however, the peculiarities of the crystalline structure of this indium selenide modification are not specified in the literature. The α- and β-In_2Se_3 polytypes have a layered structure and are considered as van der Waals or two-dimensional semiconductor compounds. The availability of α-In_2Se_3 crystals with the hexagonal (the space group P63mc) and rhombohedral (trigonal) (the space group P3m) structures, which have different geometries of connections between separate layers, dictates the necessity of dividing the α-modification into the so-called H and R (or $2H$ and $3R$) phases [20, 23]. The hexagonal α-polytype of In_2Se_3 with the deformed cation and anion sublattices in every layer (Peierls deformations) are also classified into a separate orthorhombic α'-modification [20, 24]. In work [25], α-In_2Se_3 crystals with a certain amount of helical dislocations emerging as a result of the long-term annealing at temperatures close to the melting one were proposed to be considered as a separate polytype, the so-called "vacancy ordered in screw form" (VOSF) polytype.

Quite often, the obtained In_2Se_3 samples are mixtures of various polytypes (see, for example, works [13, 24, 26]). Furthermore, In_2Se_3 samples can contain nanosized inclusions of other compounds, such as Se [26, 27], InSe [27], In_6Se_7 [27, 28], and others. The Se inclusions are mainly observed in In_2Se_3 crystals, either atomically doped or intercalated with ions of various metals [29–31]. Such crystals are identified as

a material possessing the structure of a phase belonging to the space group R3mH and the trigonal system, which may contain additional inclusions of compounds whose composition includes a doping or intercalating component. For instance, when doping In_2Se_3 with manganese, the formation of not only Se but also $MnIn_2Se_4$ inclusions was observed [29]. However, the study of the structure of such crystals is mostly limited to the registration of the presence of inclusions of other phases [29–31].

In work [27], exciton-phonon interaction in nanosized InSe inclusions in the α-In_2Se_3 layered matrix was considered. In the presence of nanosized In_6Se_7 inclusions (the gap width $E_{g(\mathrm{dir})} = (0.64 \div 0.86)$ eV for direct transitions and $E_{g(\mathrm{indir})} = 0.34$ eV for indirect ones at $T = 300$ K [32]), hexagonal α-In_2Se_3 crystals ($E_g = (1.3 \div 1.36)$ eV at $T = 300$ K [32]) acquire the properties of semiconductor structures with numerous quantum wells (semiconductor multiple-quantum-well (MQW) structures) or superlattices characterized by the current instability and the appearance of Z- and N-shaped current-voltage characteristics [28]. The aim of this research was to characterize nanostructured In_6Se_7 inclusions, the presence of which leads to the current instability in layered α-In_2Se_3 crystals, making use of several analytical X-ray diffractometry (XRD) methods.

2. Experimental Technique

In_2Se_3 crystals were grown by the Bridgman method from the stoichiometric melt at a temperature gradient of 15 K/cm at the crystallization front and a growth rate of 1 mm/h. The internal diameter of quartz ampoules was 15 mm. Crystals obtained in such a way were characterized by the n-type of conductivity ($n = (4 \div 6) \times 10^{17}$ cm^{-3} and a mobility of 400 cm^{2}V^{-1}s^{-1}) and a distinctly pronounced layered structure along the entire ingot length.

For the measurements of current-voltage characteristics (CVCs), we used samples in the form of plane-parallel plates, which were fabricated by exfoliating from a massive ingot. Indium (In) pressure contacts were used as current collectors. Note that the measurement results practically did not depend on the method used to create the In metal contacts: pressure, vacuum-sputtered, or alloying contacts.

The CVC measurements were carried out in the dc mode (the constant electric field was applied in the direction perpendicular to the In_2Se_3 layers) at temper-

atures close to room temperature. The samples were sorted according to the type of their CVCs: linear or *Z*- and *N*-shaped (Fig. 1). Then they were powdered to obtain a grain size of less that 75 μm. The crystal structures of the In$_2$Se$_3$ samples of both types were studied using the XRD method on a DRON-3 diffractometer in Cu-Kα radiation ($\lambda = 1.5418$ Å) in the Bragg angle interval of $8° < 2\theta < 60°$. The scanning increment was $0.05°$, with an exposure time of 5 s at every point. The DRON-3 instrumental errors were taken into account by studying the powders of single crystalline Si and Al$_2$O$_3$ standards.

3. Experimental Results and Their Discussion

In Fig. 2, *a*, an X-ray diffractogram of the In$_2$Se$_3$ powder obtained from crystalline samples with linear CVCs (see Fig. 1, curve *1*) is depicted. A set of diffraction maxima are observed, whose positions correspond to the α-In$_2$Se$_3$ polytype described by the space group P63/mmc(194) of hexagonal system (standard JCPDS Card No: 23-294 [33]). The measured parameters of the unit cells are $a = 4.025$ Å and $c = 19.235$ Å; they agree well with the data given in the literature [20, 34]. No other peaks were revealed which could testify to the availability of foreign crystalline phases in the material, including the abovementioned Se, InSe, and In$_6$Se$_7$ ones, as well as others. To put it differently, crystalline samples demonstrating linear CVCs were single-phase and contained only the hexagonal α-In$_2$Se$_3$ phase.

A number of additional broadened reflexes with low intensities (Fig. 2, *b*) observed in the Bragg angle interval $2\theta \approx 8° \div 20°$ in the X-ray pattern for the powder obtained from crystalline samples demonstrating *Z*- and *N*-shaped CVCs (see Fig. 1, curve *2*) testify to the presence of crystalline In$_6$Se$_7$ inclusions of monoclinic system belonging to the space group P2$_1$ (standard JCPDS Card No: 24-0070 [35]) in the hexagonal α-In$_2$Se$_3$ matrix (standard JCPDS Card No: 23-294 [33]). The crystal lattice parameters for In$_6$Se$_7$ are $a = 9.43$ Å, $b = 4.06$ Å, $c = 17.66$ Å, and $\beta = 109°$, which agree well with their counterparts given in works [36–38]. In this case, the initial crystals can be considered as a heterogeneous mixture of two crystalline phases or a two-phase composite.

In the framework of the traditional approach, the average size D_{hkl} of coherent scattering regions
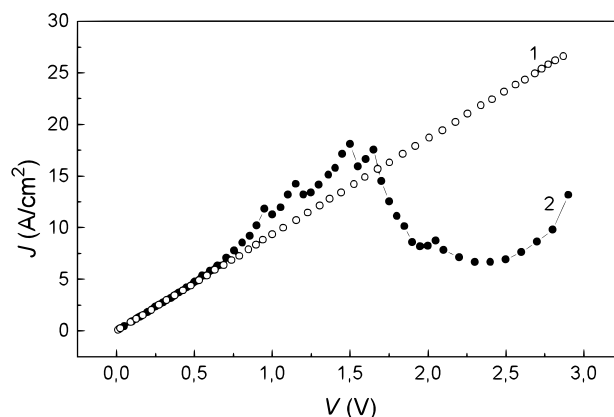
Fig. 1. Typical current-voltage characteristics (CVCs) of In$_2$Se$_3$ samples with a thickness of 600 μm at the temperature $T = 289$ K: linear (curve *1*), *Z*- and *N*-shaped (curve *2*)

(CSRs) in the crystallographic direction $[hkl]$ – in the first approximation, this parameter is considered to be equal to the average size of various nanosized particles: crystallites, grains, domains, blocks, or nanoparticles themselves – is usually determined from XRD spectra using the Scherrer equation [39]

$$D_{hkl} = \frac{K\lambda}{\beta_{(hkl)} \cos\theta_{(hkl)}}, \qquad (1)$$

where K is the Scherrer constant (for particles with the most thermodynamically advantageous rounded shape, $K = 0.9$ [40]); λ is the X-ray radiation wavelength; h, k, and l are the Miller indices; and $\theta_{(hkl)}$ is the diffraction angle ($2\theta_{(hkl)}$ is the (hkl) reflex position); whereas the linear broadening $\beta_{(hkl)}$ of the (hkl) diffraction line is given by the expression [41]

$$(\beta_{(hkl)})^n = \left[\left(B_{(hkl)}\right)^n - \left(b_{(instr)}\right)^n \right]^n, \qquad (2)$$

where $B_{(hkl)}$ is the full width at half maximum (FWHM) of (hkl) profile, and $b_{(instr)}$ is a correction for the instrumental broadening of the reflex. Depending on the mathematical functions that are chosen to describe the diffraction lines of the sample and the standard, the power exponent n in formula (2) can vary from $n = 1$, when the reflex profiles for the sample and the standard are described by the Lorentzian (Cauchy) functions, to $n = 2$, when the both profiles are described by the Gaussian functions.

Rather often, the average size of particles of various types is evaluated using the Scherrer formula applied to the broadening of a single and, as a rule, most
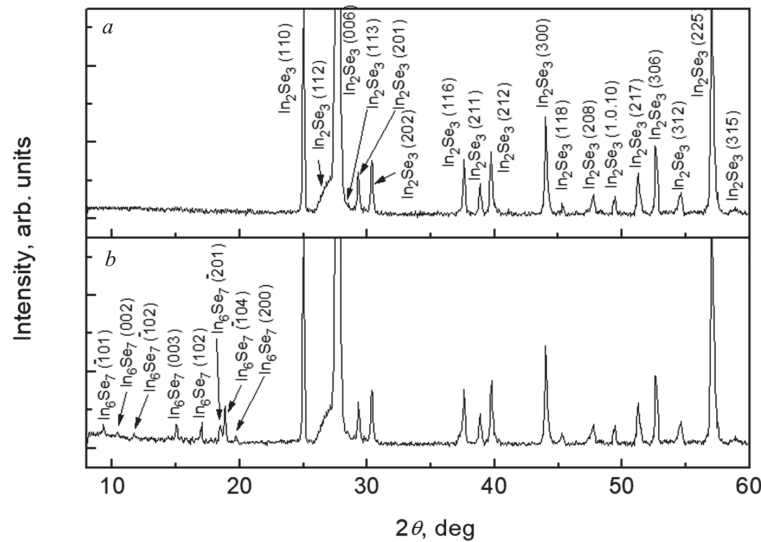
Fig. 2. X-ray diffractograms of In_2Se_3 powders obtained from crystalline samples with (*a*) linear (see Fig. 1, curve *1*) and (*b*) *Z*- and *N*-shaped (see Fig. 1, curve *2*) CVCs. Due to a large difference between by the intensities of the (110), (006), and (225) diffraction maxima for In_2Se_3 and In_6Se_7, the maxima of ordinate axes on both diffractograms correspond to about $\frac{1}{20}$ of the intensity of the In_2Se_3 peak (006)

intensive diffraction maximum (see, e.g., works [42–44]). However, actually, the particle sizes determined from different reflexes differ from one another. Therefore, in order to determine the average size D_{aver} of In_6Se_7 crystallites in the layered α-In_2Se_3 matrix accounting for all identified diffraction maxima whose intensities were 2.5 to 3 times higher than the noise level, we used the graphical solution method for the modified Scherrer equation [45, 46]

$$\ln \beta_{(hkl)} = \ln \frac{K\lambda}{D_{(hkl)}} + \ln \frac{1}{\cos \theta_{(hkl)}}. \tag{3}$$

On the other hand, the Gaussian correction was used to consider the correction for the diffractometer instrument function and X-ray geometry (the instrumental correction) when determining the val-

Parameters of In_6Se_7 nanocrystallites in the layered α-In_2Se_3 matrix determined using various X-ray diffractometry methods

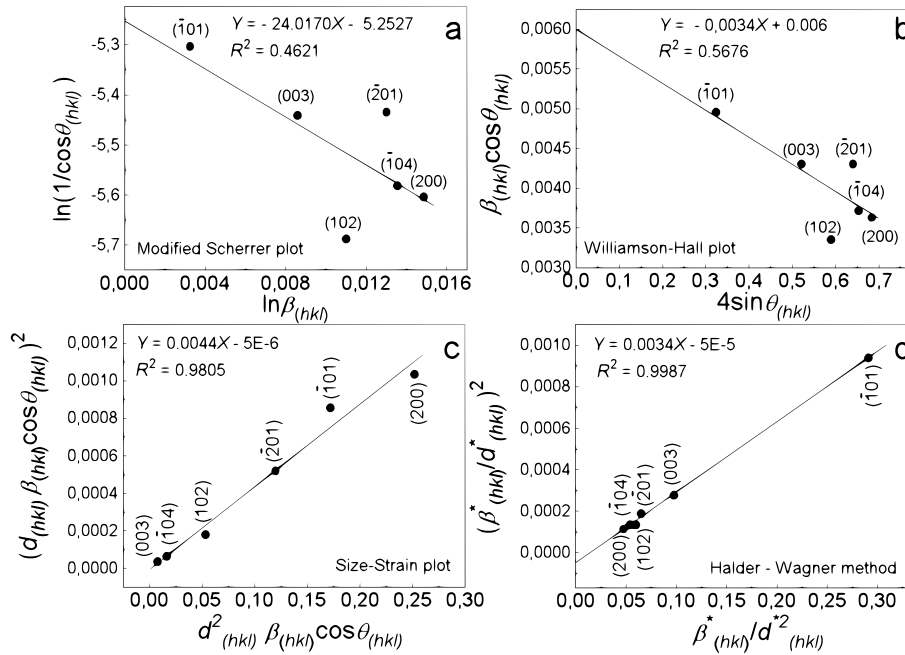| Method	D_{aver}, nm	$\varepsilon \times 10^{-3}$
Modified Scherrer	26,53	–
Williamson–Hall	23.13	−3.43
Size-Strain plot	31.54	−4.4
Halder–Wagner	26.47	−3.5

ues of $\beta_{(hkl)}$ according to formula (2). The intersection of the line $Y = AX + B$ that approximates experimental data in the coordinates $\ln \beta_{(hkl)}$ versus $\ln(1/\cos \theta_{(hkl)})$ with the ordinate axis at $\ln(1/\cos \theta_{(hkl)}) = 0$ gives a value for $\ln(K\lambda/D_{\text{aver}})$ (Fig. 3, *a*) and makes it possible to determine the average size of In_6Se_7 crystallites (the CSR size), $D_{aver} = 26.53$ nm (Table).

The average size values D_{aver} determined for nanoparticles of various kinds using the Scherrer formula are considered as evaluative ones. They correspond to real values, with an accuracy to the approximating function, if the broadening of diffraction lines in the X-ray diffractogram is induced by only the CSR dispersion. Besides the instrumental and size effects, a contribution to the width of diffraction reflexes can be made by microstrains induced in the material by defects of various types: dislocations, stacking faults, twinning, grain boundaries, subboundaries, point-defect clusters, and so forth [47].

To separate the contributions from the CSR size and the elastic deformation to the widths of (*hkl*) diffraction peaks, several approaches have been developed, which include the Warren–Averbach, Enzo, Balzar, Williamson–Hall, and others methods [48]. In the framework of the Warren–Averbach, Balzar, and Enzo methods, the profiles of a set of diffraction max-

Fig. 3. Modified Scherrer (*a*), Williamson–Hall (*b*), SSP (*c*), and Holder–Wagner (*d*) dependences plotted to characterize In_6Se_7 nanocrystallites in the layered α-In_2Se_3 matrix. R^2 is the reliability of approximation of experimental data (symbols) by the corresponding dependence (lines)

ima are considered as a convolution of the profiles of physical expansion and instrumental broadening. In turn, the function of the physical sample expansion is considered as a convolution of functions related to the CSR sizes and microdeformations. The operation of deconvolution for resolving the profile components is carried out using the Fourier transform with the help of the Voigt function in the Balzar method or the pseudo-Voigt function in the Enzo method.

If there are no diffraction maxima of different orders of X-ray radiation reflection from the same family of planes, or if their forms are not favorable for their expansion in Fourier series in order to separate between the size contribution $\beta_{(hkl)\mathrm{Size}}$ to the widths of diffraction lines and the contribution of the microstrain-induced expansion $\beta_{(hkl)\mathrm{Strain}}$ (including the case when the diffraction reflexes are weak and can equally be approximated by either the Gaussian or the Lorentzian profiles), the Williamson–Hall method is most often used [39, 46, 49, 50]:

$$\beta_{(hkl)} = \frac{K\lambda}{D_{(hkl)} \cos\theta_{(hkl)}} + 4\varepsilon \tan\theta_{(hkl)}, \qquad (4)$$

or

$$\beta_{(hkl)} \cos\theta_{(hkl)} = \frac{K\lambda}{D_{(hkl)}} + 4\varepsilon \sin\theta_{(hkl)}, \qquad (5)$$

where ε is the relative deformation value. The first term in formula (4) is the Scherrer formula, and the second one is the well-known Stokes–Wilson equation [51, 52] used to determine microstrains in crystalline materials.

The Williamson–Hall dependence for nanosized In_6Se_7 crystallites is shown in Fig. 3, *b*. For its plotting, we did not use the diffraction maxima (002) and ($\bar{1}$02) whise intensities did not exceed 2.5 times the background level (Fig. 2, *b*). The average size of nanocrystallites, $D_{\mathrm{aver}} = 23.13$ nm (Table), was calculated by extrapolating the dependence of the integral width on the scattering vector magnitude to the zero value of the latter parameter (Fig. 3, *b*). The microdeformation value $\varepsilon = -3.4 \times 10^{-3}$ (Table) was determined from the slope of this plot.

As one can see from Fig. 3, *b*, the Williamson–Hall dependence for In_6Se_7 crystallites is characterized by a negative slope coefficient, which testifies

to the availability of compressive strains in them [50, 53]. According to works [54, 55], compressive microstrains emerge in the samples in the presence of such planar defects as stacking faults. The action of compressive microstrains in In_6Se_7 crystallites leads to a certain reduction of the calculated lattice parameters (c and the angle β) in comparison with those given in the standard JCPDS Card No: 24-0070 [35], but they almost completely coincide with their counterparts for the crystals [36] and thin films [37, 38] of this compound. The origins of the decrease of the parameter c and the angle β in the In_6Se_7 crystal lattice have not been interpreted in works [36–38].

Attention is also drawn by the fact that the average size of In_6Se_7 crystallites determined in the framework of the Williamson–Hall method is smaller than the value determined using the modified Scherrer method (Table). When determining D_{aver} in the framework of the Williamson–Hall method, the action of microstrains in In_6Se_7 nanocrystallites was considered to be isotropic. A more accurate method for the determination of D_{aver} and ε, which involves the crystalline structure of nano-sized objects of various kinds, is the so-called Size-Strain plot (SSP) method [46]. In the framework of this method, it is assumed that the broadening of reflexes is described by the Lorentzian function if it occurs due to the CSR size effect, and by the Gaussian function if due to the microdeformations in the crystal lattice. This assumption allows the following equation to be used in calculations [56]:

$$\left(d_{(hkl)}\beta_{(hkl)}\cos\theta_{(hkl)}\right)^2 =$$
$$= \frac{K\lambda}{D_{(hkl)}}\left(d_{(hkl)}^2\beta_{(hkl)}\cos\theta_{(hkl)}\right) + \left(\frac{\varepsilon}{2}\right)^2, \qquad (6)$$

where a, b, c, and β are the unit call parameters, and $d_{(hkl)}$ are interplanar distances, which can be found from the following relationship for crystals of monoclinic system [57]:

$$\frac{1}{d_{(hkl)}^2} = \frac{h^2}{a^2\sin\beta} + \frac{k^2}{b^2} + \frac{l^2}{c^2\sin^2\beta} - \frac{2hl\cos\beta}{ac\sin^2\beta}. \qquad (7)$$

The average size of In_6Se_7 crystallites, $D_{aver} = 31.54$ nm (Table), was determined from the slope of the line $Y = AX + B$ that approximates the experimental data in the coordinates $(d_{(hkl)}^2\beta_{(hkl)}\cos\theta_{(hkl)})$

versus $(d_{(hkl)}\beta_{(hkl)}\cos\theta_{(hkl)})^2$ (Fig. 3, c), and the microstrain value was found from the intersection of this line with the ordinate axis (at $\cos\theta_{(hkl)} = 0$). As one can see from Fig. 3, c, the intersection point of dependence (6) with the ordinate axis has the negative ordinate value, which testifies to the availability of compressive strains in In_6Se_7 crystallites. Therefore, the strain value was determined from the absolute value of the intersection point ordinate and taking into account the direction of strain action: $\varepsilon = -0.5\sqrt{|B|} = -4.4 \times 10^{-3}$ (Fig. 3, c and Table).

Note that the SSP method is also based on the assumption that strains act isotropically in nanoparticles of various kinds. However, the application of the parameters calculated for the In_6Se_7 crystal lattice, which underwent changes only in a certain crystallographic direction owing to the action of compressive strains [formulas (6) and (7)], brings us to the conclusion that the method can automatically account for the anisotropic action of microstrains in In_6Se_7 nanocrystallites.

As is evidenced by numerous studies, the profiles of diffraction maxima in X-ray diffraction patterns obtained for nano-sized particles of various types are most correctly approximated using the symmetric Voigt function; the latter is a linear combination of the Gaussian and Lorentzian functions [49, 58]. If the experimental profile $B_{(hkl)}$ and the instrument function $b_{(instr)}$ of the (hkl) diffraction maximum are described by the Voigt function, then, in the framework of the Halder–Wagner method, the physical reflex width $\beta_{(hkl)}$ is determined by the formula [59]

$$\beta_{(hkl)} = \sqrt{\left(B_{(hkl)}\right)^2 - B_{(hkl)}b_{(instr)}}, \qquad (8)$$

and the values of D_{aver} and ε can be calculated from the relation [58, 59]

$$\left(\frac{\beta_{(hkl)}^*}{d_{(hkl)}^*}\right) = \frac{K}{D_{hkl}}\frac{\beta_{(hkl)}^*}{d_{(hkl)}^{*2}} + \left(\frac{\varepsilon}{2}\right)^2. \qquad (9)$$

where
$$\beta_{(hkl)}^* = \frac{\beta_{(hkl)}\cos\theta_{(hkl)}}{\lambda}, \quad d_{(hkl)}^* = \frac{2\sin\theta_{(hkl)}}{\lambda}.$$

The slope of the line $Y = AX + B$ that approximates the experimental data in the coordinates $\beta_{(hkl)}^*/d_{(hkl)}^{*2}$ versus $(\beta_{(hkl)}^*/d_{(hkl)}^*)^2$ is equal to $K\lambda/D_{aver}$, and its intersection with the ordinate axis

at $\beta^*_{(hkl)}/d^{*2}_{(hkl)} = 0$ makes it possible to determine the microstrain ε. As one can see from Fig. 3, *d*, the intersection point of dependence (9) and the ordinate axis, similarly to the previous case, lies on the negative side of the axis, which testifies to the availability of compressive strains in In₆Se₇ crystallites. The values $D_{\text{aver}} = 26.47$ nm and $\varepsilon = -3.5 \times 10^{-3}$, which were determined using the Holder–Wagner method, are quoted in Table. Note that, in comparison with other methods, the Holder–Wagner method provides the best agreement between the determined and real D_{aver} values if diffraction reflexes located at small angles 2θ are used for calculations [58], which actually took place in our case (Fig. 2, *b*).

As one can see from Table, the maximum average sizes of In₆Se₇ crystallites in the layered α-In₂Se₃ matrix were obtained using the SSP method. However, when this method was applied to calculate the average size of spherical nanoparticles of various kinds, the dimensionless particle shape factor $K = 3/4$ was used instead of $K = 0.9$ (see, e.g., works [60, 61]). This choice was associated with the fact that, when using the modified Scherrer method, as well as the Williamson–Hall and Holder–Wagner methods, the determined values of D_{aver} are averaged over the particle volume. In the SSP method, the transition to the averaging over the particle volumes takes place via the averaging over the surface areas of the particles. If the value $K = 3/4$ is used instead of $K = 0.9$, the average size of In₆Se₇ nanocrystallites determined in the framework of the SSP method equals 26.28 nm rather than 31.54 nm, so that the obtained value practically coincides with the D_{aver} values calculated using the modified Scherrer and Holder–Wagner methods (the difference does not exceed 2.5 Å).

The minimum average size of In₆Se₇ nanocrystallites in the α-In₂Se₃ matrix, $D_{\text{aver}} = 23.13$ nm, was obtained by applying the Williamson–Hall method (Table). It should be noted that the determination of D_{aver} for In₆Se₇ crystallites using this method was performed assuming the reflex profiles in the X-ray diffractogram to be described by the Lorentzian function [formulas (2), (4), and (5), and Fig. 3, *b*]. With this assumption, the Williamson–Hall dependence makes it possible to determine the upper limit of the D_{aver} values and the lower limit of the ε values [62]. If we assume the Gaussian shape of diffraction lines, the lower limit for D_{aver} and the upper limit for ε can be found. In other words, the maximum possible

values were obtained for the average size of In₆Se₇ nanocrystallites. However, the values of D_{aver} and ε were determined in the framework of the Williamson–Hall method using the so-called Uniform Deformation Model [60, 61]. In the latter, neither the crystalline structure nor the elastic properties of In₆Se₇ are taken into consideration.

Currently, the absence of data in the literature concerning the elasticity tensor components for In₆Se₇ does not allow the D_{aver} and ε values to be corrected with the help of other models (the Uniform Stress Deformation Model or the Uniform Deformation Energy Density Model) applied in the framework of the Williamson–Hall method. Attention is also attracted by the fact that the approximation reliability R^2 of experimental data grows among the set of dependences selected for the characterization of In₆Se₇ nanocrystallites in the following order: the modified Scherrer dependence – the Williamson–Hall dependence – the Size-Strain plot dependence – the Holder–Wagner dependence (Fig. 3). In particular, the value of the approximation reliability of experimental points is approximately equal to 46.2% for the modified Scherrer method (Fig. 3, *a*) and to almost 100% for the Holder–Wagner one (Fig. 3, *d*).

If In₆Se₇ inclusions compose a dense cluster of nanocrystallites (a grain) in the layered α-In₂Se₃ matrix, the average concentration of dislocations, δ_{out}, is determined by their average size [36],

$$\delta_{\text{out}} = \frac{1}{D^2_{\text{aver}}}, \tag{10}$$

whereas the average concentration of dislocations in separate crystallites of monoclinic system, δ_{in}, is proposed to be evaluated using the following formula [63]:

$$\delta_{in} = \frac{\beta^2_{\text{aver}}}{9(\mathbf{b})^2}. \tag{11}$$

where $\mathbf{b}$ is the Burgers vector, and β_{aver} is the averaged physical width of all identified diffraction maxima $\beta_{(hkl)}$. Taking $D_{\text{aver}} \approx 26.5$ nm, we get $\delta_{\text{out}} \approx$ $\approx 1.42 \times 10^{11}$ cm^{-2}. When calculating the average dislocation concentration $\delta_{in} = 2.42 \times 10^{9}$ cm^{-2} in In₆Se₇ nanocrystallites, the $\beta_{(hkl)}$ values determined by formula (8) were averaged over all diffraction peaks with the intensity 2.5 to 3 times higher than the background level. As the Burgers vector, the minimum translation vector was adopted, i.e., the parameter $b = 4.06$ Å for the crystal lattice in monoclinic In₆Se₇.

As one can see from Fig. 1, the initial sections (at voltages $V < 0.5$ V) in the CVCs for α-In_2Se_3 crystalline plates of the same thickness but without (curve *1*) and with (curve *2*) In_6Se_7 phase inclusions coincide. The resistivity values determined from those CVC sections are identical for the samples of both types.

The results of experimental studies [64] demonstrate that the insertion of semiconductor particles into a wide-band-gap material does not change the resistivity of the latter if the volume fraction of the filler $x_V < 0.15$. At $x_V \geq 0.15$, a transition begins from the properties of host matrix to the properties of semiconductor filler, which is accompanied changes in the wide-band-gap matrix resistivity. According to the percolation theory [65], if $x_V \geq 0.15$, the formation of a primary chain (a continuous cluster) connecting metal electrodes on the opposite surfaces of the sample, which is the disordered macrosystem "wide-band-gap matrix – semiconductor particles (filler)", becomes probable.

The aforesaid makes it possible to assert that the volume fraction of the phase consisting of the narrower-band-gap component In_6Se_7 does not exceed 15% in the In_2Se_3/In_6Se_7 samples demonstrating the current instability with the Z- and N-shaped CVCs (Fig. 1, curve *2*). In order to accurately determine the ratio between the In_2Se_3 and In_6Se_7 phases in the examined composite samples, the X-ray diffraction-absorption method for quantitative analysis was applied [66]. In the framework of this method, the concentration of phase 1 in a two-component mixture is calculated via the Klug equation

$$x_{M(1)} = \left(\frac{I_{(hkl)(1)}}{I^0_{(hkl)(1)}}\right)\left(\frac{\mu}{\rho}\right)_{(1)} \times$$
$$\times \left\{\left(\frac{\mu}{\rho}\right)_{(1)} - \left(\frac{I_{(hkl)(1)}}{I^0_{(hkl)(1)}}\right)\left[\left(\frac{\mu}{\rho}\right)_{(1)} - \left(\frac{\mu}{\rho}\right)_{(2)}\right]\right\}^{-1}, \quad (12)$$

where $x_{M(1)}$ is the mass fraction of phase 1 in the mixture; $I_{(hkl)(1)}$ and $I^0_{(hkl)(1)}$ are the intensities of the (hkl) diffraction maximum selected for calculation for phase 1 in the mixture and in the pure substance, respectively; and $(\mu/\rho)_{(1)}$ and $(\mu/\rho)_{(2)}$ are the mass absorption coefficients for phases 1 and 2, respectively, at the experimental????? wavelength.

The results of calculations using formula (12) for the In_2Se_3 Bragg reflections (110), (006), and (225) in X-ray diffraction patterns of In_2Se_3 and In_2Se_3/In_6Se_7 (Fig. 2) testify that the mass fraction of In_2Se_3 in the composite equals 0.9902. Accordingly, the mass fraction of In_6Se_7 in the mixture equals 0.0098, i.e., about 1 wt%. In the calculations, the mass absorption coefficients of In_2Se_3 (158.85 cm^2/g) and In_6Se_7 (168.72 cm^2/g) for energies corresponding to Cu-Kα radiation were determined according to the method of work [67], i.e., as weighted average values of individual mass absorption coefficients for the In and Se elements. The mass absorption coefficients of individual elements in a wide energy interval can be found in the literature (see, e.g., work [68]). By definition, the volume concentration of either of the phases in a two-component mixture (in our case, this is $x_{V(In_6Se_7)}$) is equal to the ratio between the volume of this phase, $V_{(In_6Se_7)}$, and the volume of the composite in whole,

$$x_{V(In_6Se_7)} = V_{(In_6Se_7)}/\left(V_{(In_6Se_7)} + V_{(In_2Se_3)}\right), \quad (13)$$

or, in terms of masses and densities,

$$x_{V(In_6Se_7)} = m_{(In_6Se_7)}/\rho_{(In_6Se_7)} \times$$
$$\times \left\{m_{(In_6Se_7)}/\rho_{(In_6Se_7)} + m_{(In_2Se_3)}/\rho_{(In_2Se_3)}\right\}^{-1}. \quad (14)$$

Taking a density value of 5.80 g/cm^3 for In_2Se_3 and 5.86 g/cm^3 for In_6Se_7 [32], we obtain that the volume fraction of In_6Se_7 in the studied In_2Se_3/In_6Se_7 samples was $x_{V(In_6Se_7)} = 0.00969$, which corresponds to the average concentration $n_{In_6Se_7} \approx 3.12 \times 10^{15}$ cm^{-3} of In_6Se_7 nanocrystallites with the average size $D_{aver} \approx 26.5$ nm over the layered α-In_2Se_3 matrix (more accurately, over the volume of the In_2Se_3/In_6Se_7 composite).

The phenomenological XRD methods applied to characterize In_6Se_7 nanocrystallites do not directly answer the question "Which are In_6Se_7 inclusions in In_2Se_3 crystals: separate crystallites or their clusters (grains)?" According to the results of work [69], the current instability in superlattices (including disordered ones) or semiconductor MQW structures with Z- and N-shaped CVCs is associated with resonance tunneling of charge carriers between neighbor potential wells, as well as between metal electrodes and nearest potential wells. Such a current transfer mechanism imposes restrictions not on the sizes of the narrow-band-gap phase inclusions (in our case, these are In_6Se_7 inclusions) but on the thickness of the

interlayers of the wide-band-gap phase (In$_2$Se$_3$) between neighbor inclusions, which have to be "tunnel-transparent".

On the other hand, according to the results of work [70], CVCs of this type in semiconductor MQW structures result from electron field emission and resonance electron tunneling from quantum dots onto levels in the wide-band-gap matrix, which becomes possible because of the energy quantization of charge carriers in the quantum dots. In this case, the sizes of nano-objects are subjected to restrictions because the energy quantization of charge carriers in the quantum dots occurs owing to the electric field penetration into them, which is directly related to the smallness of the particle rounding radius [70].

The implementation of such current transfer mechanisms in In$_2$Se$_3$/In$_6$Se$_7$ samples assumes the availability of In$_6$Se$_7$ inclusions in the In$_2$Se$_3$ matrix in the form of separate nanocrystallites (they provoke the current instability with Z- and N-shaped CVCs in weak fields). On the other hand, they do not exclude the simultaneous presence of inclusions of larger sizes, which are clusters of In$_6$Se$_7$ crystallites (they do not provoke the current instability in weak fields).

Finally, note that if α-In$_2$Se$_3$ crystaline samples with In$_2$Se$_3$ inclusions are illuminated with full-spectrum light, they demonstrate negative integral photosensitivity in the direction perpendicular to the layers, and positive one in the direction along the layers (the results of the study of photoconductivity in In$_2$Se$_3$/In$_6$Se$_7$ samples are being prepared for publication). The maximum of the band that is responsible for both negative and positive integral photoconductivity corresponds to the energy $h\nu \approx (0.8 \div 0.81)$ eV and its intensity esceeds the intensity of the band associated with interband transitions in In$_2$Se$_3$ by more than an order of magnitude. Furthermore, the photocurrent rise time after the light is switched on and the time of photocurrent relaxation to equilibrium dark values after the light is switched off are at least at 2 to 3 orders of magnitude shorter than the corresponding values for some polycrystalline films (see, e.g., works [71, 72]) or nanocomposites (see, e.g., works [73, 74]), which are considered as photoelectronic materials.

All the aforesaid testifies that In$_2$Se$_3$/In$_6$Se$_7$ samples are promising objects for operating in the spectral interval $\lambda = (1.3 \div 1.6)$ μm for optical communication applications [75]. This is the more so because the maximum position of the band that governs the integral photosensitivity (both negative and positive) of such samples coincides with one of three transparency windows (Telecom windows) of the standard optical fiber (the Single-mode optical fiber (SMF)). In comparison with others transparency windows, this one is characterized by the lowest signal attenuation (about 0.22 dB/km) and, as a result, is used for communication over long distances [76].

4. Conclusions

The results of the performed research allow the following conclusions to be drawn.

• Layered In$_2$Se$_3$ crystals grown by the Bridgman method from the stoichiometric melt of their components are found to be heterogeneous. Namely, some samples obtained from the same ingot contained only the hexagonal α-In$_2$Se$_3$ phase, whereas inclusions of the crystalline In$_6$Se$_7$ phase were revealed in the others.

• Single-phase α-In$_2$Se$_3$ samples in the form of plane-parallel plates demonstrated linear current-voltage characteristics. At the same time, In$_2$Se$_3$ samples with In$_6$Se$_7$ inclusions demonstrated Z- and N-shaped CVCs.

• Several phenomenological X-ray diffractometry methods, which were involved to characterize the microstructure of In$_6$Se$_7$ inclusions in the layered α-In$_2$Se$_3$ matrix, testify to the availability of compressive strains in In$_6$Se$_7$ crystallites.

• The availability of compressive microstrains in In$_6$Se$_7$ crystallites gave rise to the practical coincidence of their average size values, $D_{\mathrm{aver}} \approx 26.5$ nm, determined from the broadening of diffraction maxima by means of the modified Scherrer method, the Size-Strain Plot method, and the Holder–Wagner method, with the difference not exceeding 1%. A mismatch of about 12% between the indicated D_{aver} value and the value determined using the Williamson-Hall method is associated with the specific features of the uniform deformation model applied to analyze the In$_6$Se$_7$ diffraction lines, which neglects the crystalline structure and the elastic properties of crystallites. The absence of the data in the literature concerning the strain tensor components for In$_6$Se$_7$ does not permit the correction of the D_{aver} values using other models to be done in the framework of the Williamson–Hall method.

• The average concentration of dislocations was calculated in the case where In_6Se_7 nanocrystallites form a dense cluster in the layered α-In_2Se_3 matrix. The average concentration of dislocations in separate crystallites was also calculated.

• In the framework of the diffraction-adsorption method and using the Klug equation, the average mass and volume fractions of the In_6Se_7 phase in the researched α-In_2Se_3 samples were determined. The average concentration of In_6Se_7 nanocrystallites with the average size $D_{aver} \approx 26.5$ nm in the layered α-In_2Se_3 matrix was calculated.

• As an announcement of further research, the prospectivity of applying α-In_2Se_3 crystals with nanostructured In_6Se_7 inclusions for operating in the optical telecommunication interval was pointed out.

1. Q. Li, Y. Li, J. Gao, S. Wang, X. Sun. High performance single In_2Se_3 nanowire photodetector. *Appl. Phys. Lett.* **99**, 243105 (2011).

2. G. Almeida, S. Dogan, G. Bertoni, C. Giannini, R. Gaspari, S. Perissinotto, R. Krahne, S. Ghosh, L. Manna. Colloidal monolayer β-In_2Se_3 nanosheets with high photoresponsivity. *J. Am. Chem. Soc.* **139**, 3005 (2017).

3. Z. Zhang, J. Yang, F. Mei, G. Shen. Longitudinal twinning -In_2Se_3 nanowires for UV-visible-NIR photodetectors with high sensitivity. *Front. Optoelectron.* **11**, 45 (2018).

4. S.I. Drapak, V.V. Netyaga, Z.D. Kovalyuk. The electrical and photoelectrical properties of n-In_2Se_3–p-InSe heterostructures. *Tech. Phys. Lett.* **28**, 711 (2002).

5. N. Balakrishnan, C.R. Staddon, E.F. Smith, J. Stec. Quantum confinement in β-In_2Se_3 layers grown by physical vapour transport for high responsivity photodetectors. *2D Mater.* **3**, 025030 (2016).

6. S. Chen, X. Liu, X. Qiao, X. Wan, K. Shehzad, X. Zhang, Y. Xu, X. Fan. Facile synthesis of γ-In_2Se_3 nanoflowers toward high performance self-powered broadband γ-In_2Se_3/Si heterojunction photodiode. *Small.* **13**, 1604033 (2017).

7. S.H. Kwon, B.T. Ahn, S.K. Kim, F.O. Adurodija, K.H. Kang, K.H. Yoon, J. Song. Characterization of $CuInSe_2$ and In_xSe_y thin films by coevaporation method. *J. Korean Phys. Soc.* **31**, 796 (1997).

8. S. Kwon, B. Ahn, S. Kim, K. Yoon, J. Song. Growth of $CuIn_3Se_5$ layer on $CuInSe_2$ films and its effect on the pho-

9. tovoltaic properties of In_2Se_3/$CuInSe_2$ solar cells. *Thin Solid Films.* **323**, 265 (1998).

9. Y. Ohtake, S. Chaisitsak, A.Yamada, M. Konagai. Characterization of $ZnIn_xSe_y$ thin films as a buffer layer for high efficiency $Cu(InGa)Se_2$ thin-film solar cells. *Jpn. J. Appl. Phys.* **37**, 3220 (1998).

10. C. Julien, E. Hatzikraniotis, A. Chevy, K. Kambas. Electrical behavior of lithium intercalated layered In-Se compounds. *Mater. Res. Bull.* **20**, 287 (1985).

11. H. Peng, X.F. Zhang, R.D. Twesten, Y. Cui. Vacancy ordering and lithium insertion in III2VI3 nanowires. *Nano Res.* **2**, 327 (2009).

12. S. Yang, C.-Y. Xu, L. Yang, S.-P. Huabc, L. Zhen. Solution-phase synthesis of γ-In_2Se_3 nanoparticles for highly efficient photocatalytic hydrogen generation under simulated sunlight irradiation. *RSC Adv.* **6**, 106671 (2016).

13. R. Wanga, J. Wana, J. Jia, W. Xue, X. Hu, E. Liu, J. Fan. Synthesis of In_2Se_3 homojunction photocatalyst with and phases for efficient photocatalytic performance. *Materials & Design.* **151**, 74 (2018).

14. H. Lee, D.-H. Kang, L. Tran. Indium selenide (In_2Se_3) thin film for phase-change memory. *Mater. Sci. Eng. B.* **119**, 196 (2005).

15. A.M. Rasmussen, S.T. Teklemichael, E. Mafi, Y. Gu, M.D. McCluskey. Pressure-induced phase transformation of In_2Se_3. *Appl. Phys. Lett.* **102**, 062105 (2013).

16. W. Ding, J. Zhu, Z. Wang, Y. Gao, D. Xiao, Y. Gu, Z. Zhang, W. Zhu. Prediction of intrinsic two-dimensional ferroelectrics in In_2Se_3 and other III_2-VI_3 van der Waals materials. *Nat. Commun.* **8**, 14956 (2017).

17. C. Cui, W.-J. Hu, X. Yan, C. Addiego, W. Gao, Y. Wang, Z. Wang, L. Li, Y. Cheng, P. Li, X. Zhang, H.N. Alshareef, T. Wu, W. Zhu, X. Pan, L.-J. Li. Intercorrelated in-plane and out-of-plane ferroelectricity in ultrathin two-dimensional layered semiconductor In_2Se_3. *Nano Lett.* **18**, 1253 (2018).

18. G. Han, Z.-G. Chen, J. Drennan, J. Zou, Indium selenides: Structural characteristics, synthesis and their thermoelectric performances. *Small.* **10**, 2747 (2014).

19. L. Yang, Z.-G. Chen, M.S. Dargusch, J. Zou. High performance thermoelectric materials: progress and their applications. *Adv. Energy Mater.* **8**, 1701797, (2018).

20. S. Popovic, A. Tonejc, B. Grzeta-Plenkovic, B. Celustka, R. Trojko. Revised and new crystal data for indium selenides. *J. Appl. Cryst.* **12**, 416 (1979).

21. C. Amory, J.C. Bernede, S. Marsillac. Study of a growth instability of γ-In_2Se_3. *J. Appl. Phys.* **94**, 6945 (2003).

22. S.B. Syamala, K. Bindu, K.P. Vijayakumar, C. Sudha Kartha. Photoconductivity measurements on g-In_2Se_3 thin films. *Abstracts of the 13-th annual general meeting of materials research society of India* (Hyderabad, 2002), p. 267.

23. M. Kupers, P.M. Konze, A. Meledin, J. Mayer, U. Englert, M. Wuttig, R. Dronskowski. Controlled crystal growth of

indium selenide, In$_2$Se$_3$, and the crystal structures of α-In$_2$Se$_3$. *Inorg. Chem.* **57**, 11775 (2018).

24. J. van Landuyt, G. van Tendeloo, S. Amelinck. Phase transitions in In$_2$Se$_3$ as studied by electron microscopy and electron diffraction. *Phys. Stat. Sol. A* **30**, 299 (1975).

25. J. Ye, S. Soeda, Y. Nakamura, O. Nittono. Crystal structures and phase transformation in In$_2$Se$_3$ compound semiconductor. *Jpn. J. Appl. Phys.* **37**, 4264 (1998).

26. A. Chaiken, K. Nauka, G.A. Gibson, H. Lee, C.C. Yang. Structural and electronic properties of amorphous and polycrystalline In$_2$Se$_3$ films. *J. Appl. Phys.* **94**, 2390 (2003).

27. Yu.I. Zhirko, V.M. Grekhov, Z.D. Kovalyuk. Characterization, optical properties and electron (exciton)-phonon interaction in bulk In$_2$Se$_3$ crystals and InSe nanocrystals in In$_2$Se$_3$ confinement. *J. Nanomed. Nanosci.* **3**, JNAN-148 (2018).

28. S.I. Drapak, S.V. Gavrilyuk, Z.D. Kovalyuk. Current instability with Z- and N-shaped current-voltage characteristics in inhomogeneous In$_2$Se$_3$ crystals. *Tech. Phys. Lett.* **35**, 569 (2009).

29. V.M. Kaminskii, Z.D. Kovalyuk, A.V. Zaslonkin, V.I. Ivanov. Structure and electrical properties of In$_2$Se$_3$ Mn layered crystals. *Semiconductor Physics, Quantum Electronics & Optoelectronics* **12**, 290 (2009).

30. Z.D. Kovalyuk, V.B. Boledzyuk, Z.R. Kudrynskyi, A.D. Shevchenko. Ferromagnetism in Co-intercalated In$_2$Se$_3$ layered crystals. *Phys. Chem. Solid State.* **14**, 730 (2013).

31. V.M. Kaminskii, Z.D. Kovalyuk V.I. Ivanov. Structure and physical properties of In$_2$Se$_3\langle$Mn$\rangle$, InSe$\langle$Mn$\rangle$ and InSe$\langle$Fe$\rangle$ layered crystals. *Phys. Chem. Solid State.* **16**, 44 (2015).

32. O. Madelung. *Semiconductors: Data Handbook. 3rd Edition* (Springer, 2004) [ISBN: 978-3-540-40488-0].

33. Powder diffraction file, Joint Committee on Powder Diffraction Standards (JCPDS), JCPDS Card No: 23-294.

34. Ya-Chu Hsu, Yu-Chen Hung, Chiu-Yen Wang. Controlling growth high uniformity indium selenide (In$_2$Se$_3$) nanowires via the rapid thermal annealing process at low temperature. *Nanoscale Res. Lett.* **12**, 532 (2017).

35. Powder diffraction file, Joint Committee on Powder Diffraction Standards (JCPDS), JCPDS Card No: 24-0070.

36. R. Walther, H.J. Deiseroth. Redetermination of the crystal structure of hexaindium heptaselenide, In$_6$Se$_7$. *Zeitshrift fur Kristallographie.* **210**, 359 (1995).

37. A.F. El-Deeb, H.S. Hetwally, H.A. Shebata. Structural and electrical properties of In$_6$Se$_7$ thin films. *J. Phys. D: Appl. Phys.* **41**, 125305 (2008).

38. R. Anuroop, B. Pradeep. Structural, optical, ac conductivity and dielectric relaxation studies of reactively evaporated In$_6$Se$_7$ thin films. *JALCOM (Journal of Alloys and Compounds)* **702**, 432 (2017).

39. A.I. Gusev. *Nanomaterials, Nanostructures and Nanotechnologies* (Fizmatlit, 2005).

40. B.D. Culity, S.R. Stock. *Elements of X-Ray Diffraction. 3rd Edition* (Hentice-Hall Inc., 2001) [ISBN-10: 9789332535169].

41. E.H. Kisi, C.J. Howard. *Applications of Neutron Powder Diffraction* (Oxford University Press, 2008) [ISBN: 0199657424].

42. D. Chiche, M. Digne, R. Revel, C. Chaneac, J.-P. Jolivet D. Chiche, M. Digne, R. Revel, C. Chaneac, J.-P. Jolivet. Accurate determination of oxide nanoparticle size and shape based on X-ray powder pattern simulation: application to boehmite AlOOH Accurate determination of oxide nanoparticle size and shape based on X-ray powder pattern simulation: application to boehmite AlOOH. *J. Phys. Chem. C* **112**, 8524 (2008).

43. S. Zeinali, M. Abdollahi, S. Sabbaghi. Carboxymethyl-betta-cyclodextrin modified magnetic nanoparticles for effective removal of arsenic from drinking water: synthesis and adsorption studies. *J. Water Environ. Nanotechnol.* **1**, 104 (2016).

44. S.M. Londono-Restrepo, R. Jeronimo-Cruz, B.M. Millan-Malo, E.M. Rivera-Munoz, M.E. Rodriguez-Garcia. Efect of the nano crystal size on the X-ray difraction patterns of biogenic hydroxyapatite from human, bovine, and porcine bones. *Sci. Rep.* **9**, 5915 (2019).

45. A. Monshi, M.R. Foroughi, M.R. Monshi. Modified Scherrer equation to estimate more accurately nano-crystallite size using XRD. *WJNSE (World J. Nano Sci. Engeneering).* **2**, 154 (2012).

46. N. Rani, S. Chahal, A.S. Chauhan, P. Kumar, R. Shukla, S.K. Singh. X-ray analysis of MgO nanoparticles by modified Scherrer's, Williamson–Hall and Size-Strain method. *Materials Today: Proc.* **12**, 543 (2019).

47. R.L. Snydre, J. Fiala, H.J. Bunge. *Defect and Microstructure Analysis by Diffraction* (Oxford University Press, 1999) [ISBN: 0-19-850189-7].

48. B. Marinkovic, R.R. de Avillez, A. Saavedra, F.C.R. Assuno. A comparison between the Warren-Averbach method and alternate methods for X-ray diffraction microstructure analysis of polycrystalline specimens. *Mat. Res.* **4**, 71 (2001).

49. D. Balzar. X-ray diffraction line broadening: modeling and applications to high-Tc superconductors. *J. Res. Natl. Inst. Standart. Technol.* **98**, 321 (1993).

50. N.T. Tayade, S. Dhawakankar, P.R. Arjuwadkar. Perspective of distortion and vulnerability in structure by using the CdS-ZnS composite approach in Rietveld refinement. *J. Phys. Sci.* **22**, 137 (2017).

51. R.A.Young. *The Ritveld Method* (Oxford University Press, 1996) [ISBN: 9780198559122].

52. D. Balzar, N. Audebrand, M.R. Daymond, A. Fitch, A. Hewat, J.I. Langford, A. Le Bail, D. Louer, O. Masson, C.N. McCowan, N.C. Popa, P.W. Stephens, B.H. Toby.

Size-strain line-broadening analys is of the ceria round-robin sample. *J. Appl. Cryst.* **37**, 911 (2004).

53. P.C. de Sousa Filho, T. Gacoin, J.-P. Boilot, R.I. Walton, O.A. Serra. Synthesis and luminescent properties of REVO$_4$-REPO$_4$ (RE = Y, Eu, Gd, Er, Tm, or Yb) heteronanostructures: A promising class of phosphors for excitation from NIR to VUV. *J. Phys. Chem. C.* **119**, 24062 (2015).

54. B.E. Warren. X-ray studies of deformed metals. *Progr. Met. Phys.* **8**, 147 (1959).

55. K.R. Beyerlein, R.L. Snyder, M. Li, P. Scardi. Application of the Debye function to systems of crystallites. *Philos. Mag.* **90**, 3891 (2010).

56. J.F. Nye. *Physical Properties of Crystals – Their Representation by Tensors and Matrixes* (Clarendon Press–Oxford University Press, 1985) [ISBN-13: 978-0198511656].

57. L.M. Kovba, V.K. Trunov. *X-Ray Phase Analysis* (Moscow Univ. Press, 1976).

58. L. Motevalizadeh, Z. Heidary, M.E. Abrishami. Facile template-free hydrothermal synthesis and microstrain measurement of ZnO nanorods. *Bull. Mater. Sci.* **37**, 397 (2014).

59. N.C. Halder, C.N.J. Wagner. Separation of particle size and lattice strain in integral breadth measurements. *Acta Crystallogr.* **20**, 312 (1966).

60. R. Rai, T. Triloki, B.K. Singh. X-ray diffraction line profile analysis of KBr thin films. *Appl. Phys. A.* **122**, 774 (2016).

61. K. Manikandan, S. Dhanuskodi, A.R. Thomas, N. Maheswari, G. Muralidharan, D. Sastikumar. Size-Strain distribution analysis of SnO$_2$ nanoparticles and it's multifunctional applications of fiber optic gas sensor, supercapacitor and optical limiter. *RSC Adv.* **6**, 90559 (2016).

62. S.S. Pushkarev, M.M. Grekhov, N.V. Zenchenko. X-ray diffraction analysis of features of the crystal structure of GaN/Al$_{0.32}$Ga$_{0.68}$N HEMT-heterostructures by the Williamson–Hall method. *Semiconductors.* **52**, 734 (2018).

63. R. Yazici, D. Kalyon. Microstrain and defect analysis of CL-20 crystals by novel X-ray methods. *J. Energ. Mat.* **23**, 43 (2005).

64. V.A. Sotskov. Experimental study of the concentration dependence of resistivity in disordered macrosystems of the insulator-semiconductor type. *Tech. Phys. Lett.* **30**, 461 (2004).

65. J.M. Ziman. Models of disorder. *The Theoretical Physics of Homogeneously Disordered Systems* (Cambridge University Press, 1985) [ISBN-13: 978-0521292801].

66. S. Popovi. Quantitative phase analysis by X-ray diffraction-doping methods and applications. *Crystals.* **10**, 27 (2020).

67. B.D. Cullity. *Elements of X-Ray Diffraction. 2nd Edition* (Addison-Wesley Publishing Company, Reading, 1978) [ISBN: 9780201011746].

68. J.H. Hubbell, S.M. Seltzer. X-ray mass attenuation coefficients. NIST Standard Reference Database 126 (Tables of X-ray mass attenuation coefficients and mass energy-absorption coefficients from 1 keV to 20 MeV for elements $Z = 1$ to 92 and 48 additional substances of dosimetric interest). Last update to data content: July 2004.

69. O.V. Pupysheva, A.V. Dmitriev, A.A. Ferajian, H. Mizuseki, Y. Kowazoe. Transition between N- and Z-sharped current-voltage characteristics in semiconductor multiple-quantum-well structures. *J. Appl. Phys.* **100**, 033718 (2006).

70. A.A. Dadykin, Yu.N. Kozyrev, A.G. Naumovets. Field electron emission from Ge-Si nanostructures with quantum dots. *JETP Lett.* **76**, 472 (2002).

71. M.A. Jafarov, E.F. Nasirov, S.A. Mamedova. Negative photoconductivity of alloys of II–VI compounds. *Semiconductors.* **48**, 570 (2014).

72. A.K. Akimov, A.E. Klimov, S.V. Morozov, S.P. Suprun, Y.S. Epov, A.V. Ikonnikov, M.A. Fadeev, V,V. Rumyantsev. Giant negative photoconductivity of PbTe : In films with cut off wavelength near 30 m. *Semiconductors.* **50**, 1684 (2016).

73. S. Panigrahi, D. Basak. Morphology driven ultraviolet photosensitivity in ZnO–CdS composite. *J. Colloid Interf. Sci.* **364**, 10 (2011).

74. P. Maity, S.V. Singh, S. Biring, B.N. Pal, A.K. Ghosh. Selective near infrared (NIR) sensitive photodetector fabricated with colloidal CdS:Co quantum dots. *J. Mater. Chem. C* **7**, 7725 (2019).

75. N.B. Nahet. *Photodetectors. Materials, Devices and Applications* (Elsevier Science–Woodhead Publishing, 2016) [ISBN: 9780081027950].

76. N. Massa. *Fiber Optic Telecommunication* (SPIE, 2000).

С.І. Драпак, С.В. Гаврилюк,
Ю.Б. Халавка, В.Д. Фотій, П.М. Фочук, О.І. Федів

ХАРАКТЕРИСТИКА НАНОСТРУКТУРОВАНИХ
ВКЛЮЧЕНЬ In$_6$Se$_7$ В ШАРУВАТИХ КРИСТАЛАХ
α-In$_2$Se$_3$ АНАЛІТИЧНИМИ МЕТОДАМИ
РЕНТГЕНІВСЬКОЇ ДИФРАКТОМЕТРІЇ

Методом Бріджмена із стехіометричного розплаву компонентів вирощено шаруваті кристали In$_2$Se$_3$, які, по даним рентгеноструктурного аналізу, є неоднорідними: частина зразків, отриманих із одного і того ж зливку, містять у собі лише фазу гексагонального α-In$_2$Se$_3$, а в іншій частині виявлено включення кристалічної фази In$_6$Se$_7$. Вкраплення більш вузькозонного напівпровідника в матрицю α-In$_2$Se$_3$ спричиняють струмову нестабільність із Z- і N-подібними вольт-амперними характеристиками, в той час як однофазні зразки характеризуються лінійними залежностями струму від прикладеної напруги. Низка аналітичних методів рентгенівської дифрактометрії, залучених для встанов-

лення структури включень In_6Se_7, засвідчує в них дію стискувальних напружень, через яку середні значення розміру кристалітів In_6Se_7, визначені за допомогою модифікованого методу Шеррера, графічного розмірно-деформаційного методу і методу Холдера–Вагнера з точністю, кращою ніж 1%, співпадають і становлять 26,5 нм. Обговорюються причини неспівпадіння середнього розміру нанокристалітів In_6Se_7, визначеного за методом Вільямсона–Холла (23,13 нм), із вищезазначеними розмірами. За допомогою дифракційно-адсорбційного методу знайдено середню масову частку фа-

зи In_6Se_7 в досліджуваних зразках α-In_2Se_3 і, відповідно, розраховано середню концентрацію нанокристалітів In_6Se_7 із середнім розміром 26,5 нм у шаруватій α-In_2Se_3. Вбачається перспективність використання композитних зразків In_2Se_3/In_6Se_7 для роботи в оптичному телекомунікаційному діапазоні довжин хвиль.

Ключові слова: шаруваті кристали In_2Se_3, мікроструктура, включення нанокристалітів, композити, аналітичні методи рентгенівської дифрактометрії.